

Feasibility study on extracting the gluon polarization in Di-Jet production in polarized pp collisions at RHIC

by

Robert C. Haussman

Submitted to the Department of Physics in partial fulfillment of the requirements for the degree of

Bachelor of Science in Physics

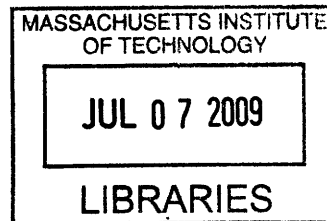
at the

MASSACHUSETTS INSTITUTE OF TECHNOLOGY

June 2009

© Robert C. Haussman, MMIX. All rights reserved.

The author hereby grants to MIT permission to reproduce and distribute publicly paper and electronic copies of this thesis document in whole or in part.



ARCHIVES

Author Department of Physics
May 21, 2009
Certified by Bernd Surrow
Assistant Professor, Department of Physics
Thesis Supervisor
Accepted by David Pritchard
Senior Thesis Coordinator, Department of Physics

Feasibility study on extracting the gluon polarization in Di-Jet production in polarized pp collisions at RHIC

by

Robert C. Haussman

Submitted to the Department of Physics
on May 21, 2009, in partial fulfillment of the
requirements for the degree of
Bachelor of Science in Physics

Abstract

The STAR experiment at the Relativistic Heavy-Ion Collider (RHIC) at Brookhaven National Laboratory (BNL) is carrying out a spin physics program at $\sqrt{s} = 200 - 500$ GeV to gain a deeper insight into the spin structure and dynamics of the proton. These studies provide fundamental tests of Quantum Chromodynamics (QCD).

One of the main objectives of the STAR spin physics program is the determination of the polarized gluon distribution function through a measurement of the longitudinal double-spin asymmetry, A_{LL} , for various processes. Di-Jet production is of particular interest since it allows a direct access of the underlying partonic kinematics, in particular the reconstruction of the gluon momentum fraction relative to the respective proton momentum.

The main objective of this study is to examine to what extent the gluon polarization can be measured as a function of the gluon momentum fraction in leading-order perturbation theory. We propose a leading order method to extract the gluon polarization from A_{LL} , and find that it transforms the problem into simply solving the quadratic formula.

Thesis Supervisor: Bernd Surrow

Title: Assistant Professor, Department of Physics

Acknowledgments

First and foremost I wish to thank Professor Bernd Surrow for both giving me this opportunity and providing the guidance and support that finally led to this completed work. I am indebted to him for many of the great ideas presented in this study. Additionally, I would like to thank MIT for their endless sources of help and inspiration – it has been a difficult four years, but perhaps the best years of my life.

Contents

1	Introduction	13
1.1	The proton spin crisis	13
1.2	Spin physics at RHIC	14
1.3	Polarized gluon distribution extraction	15
1.4	Notation	16
2	Kinematics of Di-Jet events	19
2.1	Hard-scattering model	19
2.2	Mandelstam variables	21
2.3	Di-Jet Kinematics	22
2.4	Summary	26
3	A LO Δg extraction method in Di-Jet events	31
3.1	Polarized collisions and spin asymmetry	31
3.2	Contributions from partonic spin asymmetry	33
3.3	Extraction of Δg from partonic asymmetry	35
4	Summary and further work	41

List of Figures

1-1	Upper row: $x\Delta g(Q^2 = 10 \text{ GeV})$ from the global NLO QCD analysis by DSSV [6] (left) and partial contributions $\Delta\chi_i^2$ of the fitted data sets to the total χ^2 variation of $\int_{0.05}^{0.2} \Delta g(x) dx$. The uncertainty bands correspond to $\Delta\chi^2 = 1$ (green/cross-hatched) and $\Delta\chi^2/\chi^2 = 2\%$ (yellow/vertically hatched). Previous analyses from GRSV [11] and DNS [5] are also shown. Lower panels: same as upper, but with errors scaled down by a factor of 4 as expected from the next long RHIC pp run at 200 GeV. (Taken from [7])	15
2-1	Hard scattering parton model. Two incoming hadrons of four-momentum \vec{P}_1 and \vec{P}_2 scatter via interactions between partons with distributions $f_i(x_1, \mu^2)$ and $f_j(x_2, \mu^2)$ respectively, where x_1 and x_2 are the momentum fractions of the parent hadrons and μ is the factorization scale. The interaction of the partons is given by the scattering cross section $\hat{\sigma}_{ij}(\alpha)$, where α is corresponding coupling. The product partons (represented by solid lines) are later detected indirectly through various interactions and fragmentation, from which we assume the parton subprocess can be reconstructed.	20
2-2	Mandelstam variable momentum labeling	21
2-3	Four-momentum representations in CM frame.	22
2-4	Plot of the (scaled) momentum fractions x_1 and x_2 against pseudorapidity η_3 . We only plot against η_3 as the expressions are invariant under the exchange of pseudorapidities.	27

2-5	Plot of the (scaled) invariant mass M/\sqrt{s} against the full range of x_1 . We only plot against x_1 as the expression for M is invariant under the exchange x_1 and x_2	28
2-6	Plot of the cosine of the CM scattering angle θ^* against the observed pseudorapidities.	29
2-7	Plot of the observed sum of pseudorapidities against the momentum fractions x_1 and x_2	30
3-1	Plot of the (massless) partonic asymmetry \hat{a}_{LL} against cosine of CM scattering angle θ^* for each given class of processes A, B, C, D, and E (see Table 3.1). Each line gives the relative weight towards the total spin asymmetry A_{LL}	34
3-2	Relative contributions and geometries for various classes of processes for given key angles. Note that the (massless) Di-Jet system produces symmetric product jets 180° apart (not shown).	35
3-3	Plot of the (massless) partonic asymmetry \hat{a}_{LL} against the pseudo- rapidity η_3 for several different values of η_4 for the given classes of processes (defined in Table 3.1).	36
3-4	Plots of A_{LL} against the invariant mass M/\sqrt{s} for Di-Jets at $\sqrt{s} =$ 200 GeV (upper) and $\sqrt{s} = 500$ GeV (lower), highlighting the statis- tical precision given various geometrical configurations. (From [7]) . .	37

List of Tables

3.1	Listed above are the (massless) partonic asymmetries, given in terms of Mandelstam variables and the CM scattering angle θ^* , for each given class of processes. The relative contributions to the total spin asymmetry for a given geometry are shown in Fig. 3-1, and more explicitly in Fig. 3-2.	33
-----	--	----

Chapter 1

Introduction

1.1 The proton spin crisis

The spin structure of the proton is one of the most surprising and exciting open problems in Quantum Chromodynamics (QCD). The concept of spin itself causes a rift in our intuition in that the notion of a perpetual angular momentum defies logic in the macroscopic world, yet most of the common particles, such as electrons and protons, exhibit it. With most of the properties of spin worked out 1920s, most physicists have become comfortable with the concept of spin, but it has still managed to produce interesting and unexpected surprises.

One such surprise resulted from the study of the proton. Understood as consisting of quarks, antiquarks, and gluons, it was expected that the majority of the total spin of the proton, $1/2$, must be carried by its three valence quarks. However, in the 1980s and 90s, deep inelastic scattering (DIS) experiments showed, and confirmed, that only about a third of the total spin is carried by the intrinsic spin of its constituents [9, 3]. This result, often referred to as the “proton spin crisis,” indicates that a large portion of the proton spin must be somehow divided among the orbital angular momentum of the partons (constituents of the proton) and the spins of the gluons. The implication that the spins of the gluons contribute significantly to the proton spin is a rather interesting and intriguing prospect as there are no satisfactory models of the proton that can predict the polarized gluon distribution.

The proton spin problem has spurred many theoretical and experimental efforts at facilities such as CERN, RHIC, and SLAC to map out and characterize the individual parton spin and angular momentum contributions to the proton's total spin. In particular, the RHIC facility houses the first polarized collider, which should greatly improve both the scope and accuracy of the extracted polarized parton information.

1.2 Spin physics at RHIC

The core goal of the RHIC spin program is to obtain a deeper understanding of the spin structure and dynamics of the proton in polarized proton-proton collisions [4]. Shedding light on the proton spin problem by providing insight on how the intrinsic spin of the proton is distributed among its underlying constituents of quarks, anti-quarks and gluons is an important aspect of the program. Determination of the parton orbital angular momentum contributions and gluon helicity distribution are essential for a complete understanding of the proton spin.

The polarized collider at RHIC provides collisions of transverse and longitudinally polarized proton beams at a center-of-mass energy $\sqrt{s} = 200$ GeV, and in the near future $\sqrt{s} = 500$ GeV.

The longitudinal STAR spin physics program profits enormously from the unique capabilities of the STAR experiment for large acceptance jet production, identified hadron production, and photon production [10]. The measurement of the gluon polarization through inclusive measurements such as jet production and π^0 production has been so far the prime focus of the physics analysis program [2, 1, 15]. These results provide to date the largest constraint on the gluon polarization. All measurements so far are carried out by averaging over the gluon momentum fraction. This is a feature of inclusive measurements. Correlation measurements, such as di-jet production, provides sensitivity to the underlying partonic kinematics beyond inclusive measurements, which simply integrate over the measured kinematic region.

Some important results originating partly from RHIC data have been the full global analysis at next-to-leading order (NLO) of available spin-dependent data,

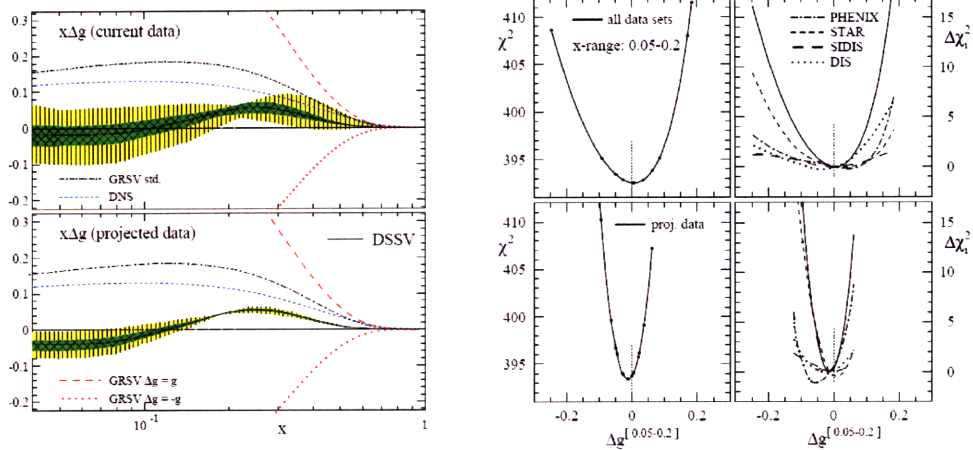


Figure 1-1: Upper row: $x\Delta g(Q^2 = 10 \text{ GeV})$ from the global NLO QCD analysis by DSSV [6] (left) and partial contributions $\Delta\chi_i^2$ of the fitted data sets to the total χ^2 variation of $\int_{0.05}^{0.2} \Delta g(x) dx$. The uncertainty bands correspond to $\Delta\chi^2 = 1$ (green/cross-hatched) and $\Delta\chi^2/\chi^2 = 2\%$ (yellow/vertically hatched). Previous analyses from GRSV [11] and DNS [5] are also shown. Lower panels: same as upper, but with errors scaled down by a factor of 4 as expected from the next long RHIC pp run at 200 GeV. (Taken from [7])

shown in Fig. 1.2 [7]. This analysis was able to constrain the polarized gluon distribution $\Delta g(x)$ over the range $0.05 < x < 0.2$, where x is the momentum fraction of the proton carried by the gluon. With only such a small range analyzed, it is obvious there is much work to still be done.

1.3 Polarized gluon distribution extraction

As mentioned in the previous section, most of the constraints on the polarized gluon distribution Δg have been the result of inclusive measurements, which inherently do not permit direct sensitivity to the actual x -dependence. This provides the motivation to pursue correlation measurements to refine the x -dependence on the parton distributions. In this work we will consider Di-Jet production, from which correlation measurements, in particular the longitudinal spin asymmetry, can better constrain the parton kinematics and hence constrain the shape of Δg . At leading order (LO), the extraction of Δg from Di-Jets would allow for a model-independent way to con-

strain the x -dependence without making any initial assumptions on the functional form of Δg (unlike what is required by global analysis). The feasibility of such a LO extraction has not yet been demonstrated. This study will be the first to demonstrate the feasibility of an experimental driven scheme to extract the momentum dependence of the gluon polarization based on Di-Jet production.

In order to work out a method of extracting Δg from the spin asymmetry A_{LL} , we first need to define and construct a set of experimentally accessible variables. This is done in Chapter 2, in which general parton kinematics are explored. Chapter 3 deals with the heart of the extraction process by first exploring the relevant quantities, namely the partonic spin asymmetry, and then exploiting a particular combination of variables to give an method through which we can extract the gluon polarization distribution.

1.4 Notation

Throughout this analysis, will work in units such that $\hbar = c = 1$. In this system

$$[\text{Length}] = [\text{Time}] = [\text{Energy}]^{-1} = [\text{Mass}]^{-1}.$$

We will use the Minkowski metric $g_{\mu\nu} = g^{\mu\nu}$ with signature $(+, -, -, -)$. We label tensors and four-vectors with Greek indices running over all spacetime components, and Roman indices running over purely spatial components. Four-vectors are represented in italic type with either a Greek index or an arrow, and three-vectors (or two-vectors in a given context) in boldface type. One-forms will be indicated with a lowered index. When providing explicit components of a four-vector, we use “ \doteq ” instead of “ $=$ ” to indicate that it takes the specific representation in the given frame or coordinate system.¹ Furthermore, we follow the Einstein summation convention of

¹This convention for four-vectors is not quite standard for particle physics, wherein four-vectors are often labeled simply with italic font (like normal variables), but in my opinion it provides more clarity.

a repeated index indicating an implied sum. For example,

$$\vec{u} = u^\mu \doteq (u^0, \mathbf{u}), \quad u_\mu = g_{\mu\nu} u^\nu = \sum_{\nu=0}^4 g_{\mu\nu} u^\nu \doteq (u^0, -\mathbf{u});$$

$$\vec{u} \cdot \vec{v} = u^\mu v_\mu = g_{\mu\nu} u^\mu v^\nu = u^0 v^0 - \mathbf{u} \cdot \mathbf{v}.$$

Finally, we distinguish between hadronic and partonic quantities by labeling those associated with partons with a hat (e.g. \hat{s}).

Chapter 2

Kinematics of Di-Jet events

This chapter presents and derives all the relevant, experimentally accessible kinematic variables necessary for the analysis. The important results are summarized at the end along with plots to explicitly show their behavior. For more information see [8, 12, 13]

2.1 Hard-scattering model

As discussed in the Introduction, the primary goal is to precisely determine the spin-dependent gluon distribution $\Delta g(x)$ over a wide range in the gluon momentum fraction x . We do so by considering the hard scattering between two hadrons in the parton model shown in Fig. 2-1. In this model, two incoming hadrons of four-momentum \vec{P}_1 and \vec{P}_2 behave as a beam of quarks and gluons, with the hard-scattering process the result of the interaction between respective partons. In the case of Di-Jets, we consider the interaction of one parton from each parent hadron with momenta $x_1\vec{P}_1$ and $x_2\vec{P}_2$ respectively, where x_i are the corresponding momentum fractions, interacting to produce two partons of momenta \vec{p}_3 and \vec{p}_4 , which later subsequently interact or fragment until detected. As mentioned in the figure caption, we assume the parton subprocess can be reconstructed from the various detections and measurements in the collider. For the characteristic hard scale Q , this process has the scattering cross

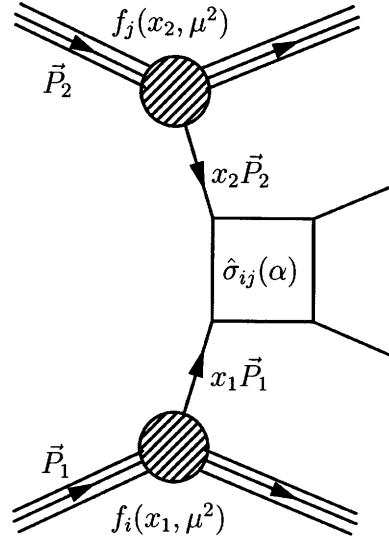


Figure 2-1: Hard scattering parton model. Two incoming hadrons of four-momentum \vec{P}_1 and \vec{P}_2 scatter via interactions between partons with distributions $f_i(x_1, \mu^2)$ and $f_j(x_2, \mu^2)$ respectively, where x_1 and x_2 are the momentum fractions of the parent hadrons and μ is the factorization scale. The interaction of the partons is given by the scattering cross section $\hat{\sigma}_{ij}(\alpha)$, where α is corresponding coupling. The product partons (represented by solid lines) are later detected indirectly through various interactions and fragmentation, from which we assume the parton subprocess can be reconstructed.

section

$$\sigma(\vec{P}_1, \vec{P}_2) = \sum_{i,j} \int dx_1 dx_2 f_i(x_1, \mu^2) f_j(x_2, \mu^2) \hat{\sigma}_{ij}(\vec{p}_1, \vec{p}_2, \alpha(\mu^2), Q^2/\mu^2), \quad (2.1)$$

where $\vec{p}_1 = x_1 \vec{P}_1$ and $\vec{p}_2 = x_2 \vec{P}_2$, and μ is the *factorization scale* – a parameter that differentiates between long and short-distance physics, usually on the order of Q for the hard-scattering process.

For high-energy (i.e. short-distance) hard scattering, the coupling is small, and hence the cross section $\hat{\sigma}$ can be expanded into a perturbation series in α

$$\hat{\sigma} = \alpha^k \sum_{m=0}^n c^{(m)} \alpha^m, \quad (2.2)$$

for some functions $c^{(m)}$. For leading-order (LO), $n = 0$, the partonic cross sections

are easily calculable. Additionally, due to asymptotic freedom, higher order approximations for this short-distance cross section can be shown to be independent of the particular details of the incoming hadrons [8].

2.2 Mandelstam variables

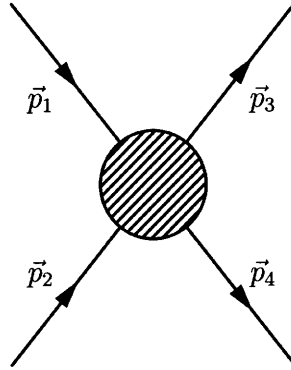


Figure 2-2: Mandelstam variable momentum labeling

In the case of Di-Jets, the process is essentially 2-body \rightarrow 2-body. Labeling the momenta as in Fig. 2-2, we can simplify many of the expressions in Di-Jet kinematics by defining the *Mandelstam variables*:

$$s = (\vec{p}_1 + \vec{p}_2)^2 = (\vec{p}_3 + \vec{p}_4)^2 \quad (2.3)$$

$$t = (\vec{p}_1 - \vec{p}_3)^2 = (\vec{p}_2 - \vec{p}_4)^2 \quad (2.4)$$

$$u = (\vec{p}_2 - \vec{p}_3)^2 = (\vec{p}_1 - \vec{p}_4)^2 \quad (2.5)$$

Examining the first variable s in more detail, we see

$$\begin{aligned} (\vec{p}_1 + \vec{p}_2)^2 &= m_1^2 + m_2^2 + 2E_1E_2 - 2\mathbf{p}_1 \cdot \mathbf{p}_2 \\ &= m_1^2 + m_2^2 + 2E_1E_2 - 2|\mathbf{p}_1||\mathbf{p}_2|\cos\theta_{12}, \end{aligned}$$

where θ_{12} is the angle between the beam directions in the given frame. The t and u variables take on similar forms. From these definitions, it is straightforward to show

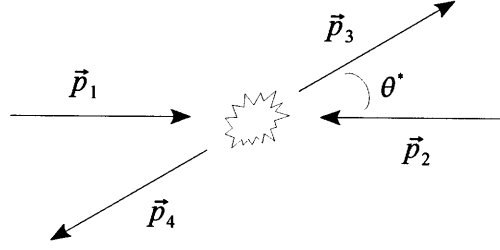


Figure 2-3: Four-momentum representations in CM frame.

the identity

$$s + t + u = \sum_{i=1}^4 m_i^2. \quad (2.6)$$

For the scattering of identical particles of mass m , the Mandelstam variables take on a particularly simple form. In the center-of-mass (CM) frame, we can write

$$\vec{p}_1 \doteq (E, p \hat{z}), \quad \vec{p}_2 \doteq (E, -p \hat{z}), \quad \vec{p}_3 \doteq (E, \mathbf{p}), \quad \vec{p}_4 \doteq (E, -\mathbf{p})$$

(see Fig. 2-3). In this configuration, the definitions lend themselves immediately to the following expressions:

$$s = (2E)^2 = E_{\text{CM}}^2, \quad (2.7)$$

$$t = -p^2 \sin^2 \theta^* - p^2 (\cos \theta^* - 1)^2 = -2p^2 (1 - \cos \theta^*), \quad (2.8)$$

$$u = -p^2 \sin^2 \theta^* - p^2 (\cos \theta^* + 1)^2 = -2p^2 (1 + \cos \theta^*). \quad (2.9)$$

These expressions are very useful for high-energy kinematics, in which we take the limit of massless partons (in this limit $p \approx E$).

2.3 Di-Jet Kinematics

Consider again the 2-body \rightarrow 2-body subprocess in Fig. 2-1. The analysis of the interaction is most easily done in the CM frame, so it is useful to parameterize the four-momenta in terms of quantities that transform simply under longitudinal boosts.

Following convention, we introduce the *rapidity* y , transverse momentum p_T , and azimuthal angle ϕ , where rapidity is defined by

$$y = \frac{1}{2} \ln \left(\frac{E + p_z}{E - p_z} \right) \quad (2.10)$$

and is additive under boosts along the z direction. For a particle (parton) of mass m and four-momentum $\vec{p} \doteq (E, \mathbf{p})$, we can represent \vec{p} in terms of the new variables by

$$\vec{p} \doteq (m_T \cosh y, p_T \sin \phi, p_T \cos \phi, m_T \sinh y), \quad (2.11)$$

where $m_T = \sqrt{p_T^2 + m^2}$. For high energy processes, we can take $m \rightarrow 0$. In this limit, $E \approx |\mathbf{p}|$ and

$$\begin{aligned} \sqrt{\frac{|\mathbf{p}| - p_z}{|\mathbf{p}| + p_z}} &= \frac{\sqrt{|\mathbf{p}|^2 - p_z^2}}{|\mathbf{p}| + p_z} = \frac{p_T}{|\mathbf{p}| + p_z} = \frac{1}{|\mathbf{p}|/p_T + p_z/p_T} \\ &= \left(\frac{1}{\sin \theta} + \frac{1}{\tan \theta} \right)^{-1} = \frac{\sin \theta}{1 + \cos \theta} = \tan(\theta/2), \end{aligned}$$

where θ is the angle from the beam as measured in the lab. Hence, the rapidity is often replaced by the *pseudorapidity*

$$\eta = -\ln \tan(\theta/2). \quad (2.12)$$

Now, consider 2-body pp collisions. In the CM frame, we can write the proton momenta as

$$\vec{P}_1 \doteq (E, 0, 0, P), \quad \vec{P}_2 \doteq (E, 0, 0, -P).$$

In the high-energy limit, $E \approx P$ and

$$\vec{P}_1 \doteq (E, 0, 0, E), \quad \vec{P}_2 \doteq (E, 0, 0, -E). \quad (2.13)$$

In this frame, the momenta of the partons are given as fractions of their respective

parent hadron's momentum

$$\vec{p}_1 = x_1 \vec{P}_1, \quad \vec{p}_2 = x_2 \vec{P}_2 \implies \vec{P}_{\text{CM}} \doteq ((x_1 + x_2)E, 0, 0, (x_1 - x_2)E). \quad (2.14)$$

From \vec{P}_{CM} we can compute the invariant mass

$$M^2 \equiv \vec{P}_{\text{CM}} \cdot \vec{P}_{\text{CM}} = (x_1 + x_2)^2 E^2 - (x_1 - x_2)^2 = 4x_1 x_2 E^2 = x_1 x_2 s = \hat{s}, \quad (2.15)$$

where we have used that the total energy $E_{\text{tot}} = 2E = \sqrt{s}$. The momenta of the outgoing partons are given by

$$\vec{p}_3 \doteq (E_3, \mathbf{p}_T, p_{3,z}), \quad \vec{p}_4 \doteq (E_4, -\mathbf{p}_T, p_{4,z}),$$

or parameterized as above

$$\vec{p}_3 \doteq (m_{3,T} \cosh y_3, \mathbf{p}_T, m_{3,T} \sinh y_3), \quad \vec{p}_4 \doteq (m_{4,T} \cosh y_4, -\mathbf{p}_T, m_{4,T} \sinh y_4).$$

In the case of large transverse momentum, $m_{i,T} = \sqrt{p_T^2 + m_i^2} \approx p_T$, and

$$\vec{P}'_{\text{CM}} = \vec{p}_3 + \vec{p}_4 \doteq (p_T(\cosh y_3 + \cosh y_4), 0, 0, p_T(\sinh y_3 + \sinh y_4)). \quad (2.16)$$

By conservation of momentum, $\vec{P}_{\text{CM}} = \vec{P}'_{\text{CM}}$, which gives

$$(x_1 + x_2)E = p_T(\cosh y_3 + \cosh y_4)$$

$$(x_1 - x_2)E = p_T(\sinh y_3 + \sinh y_4).$$

Solving for x_1 and x_2 , we find

$$x_{1,2} = \frac{p_T}{2E} \{(\cosh y_3 \pm \sinh y_3) + (\cosh y_4 \pm \sinh y_4)\}.$$

Recalling that $\cosh y_i = (e^{y_i} + e^{-y_i})/2$ and $\sinh y_i = (e^{y_i} - e^{-y_i})/2$, we find the

momentum fractions to be

$$x_1 = \frac{1}{2}x_T (e^{y_3} + e^{y_4}), \quad x_2 = \frac{1}{2}x_T (e^{-y_3} + e^{-y_4}), \quad (2.17)$$

where we have used $x_T = p_T/2E = 2p_T/\sqrt{s}$.

Now, we relate these values to those measured explicitly in the laboratory. Let \bar{y} be the total rapidity of the Di-Jet system as measured in the laboratory, and let $\pm y^*$ be the equal and opposite rapidities in the parton-parton CM frame. In terms of the measured rapidities, \bar{y} and y^* become

$$\bar{y} = \frac{1}{2}(y_3 + y_4), \quad y^* = \frac{1}{2}(y_3 - y_4) \quad (2.18)$$

For a high-energy Di-Jet with outgoing total momentum parameterized in the CM frame as

$$\vec{P}'_{\text{CM}} \doteq (p_T \cosh y^*, \mathbf{p}_T, p_T \sinh y^*),$$

we can relate the CM scattering angle θ^* to the observed rapidities via

$$\cos \theta^* \approx \frac{p_z^*}{E^*} = \frac{\sinh y^*}{\cosh y^*} = \tanh \left(\frac{y_3 - y_4}{2} \right). \quad (2.19)$$

The longitudinal parton momentum fractions can also be related to the observed rapidities by combining terms in Eq. (2.17).

$$x_{1,2} = \frac{1}{2}x_T (e^{\pm y_3} + e^{\pm y_4}) = \frac{1}{2}x_T e^{\pm(y_3+y_4)/2} (e^{(y_3-y_4)/2} + e^{-(y_3-y_4)/2}) = x_T e^{\pm \bar{y}} \cosh y^*$$

Dividing x_1 by x_2 yields $e^{2\bar{y}}$, so it follows that

$$\bar{y} = \frac{1}{2} \ln(x_1/x_2). \quad (2.20)$$

Finally, using equations (2.7)-(2.9) in the limit that $m \rightarrow 0$, the Mandelstam variables

for the Di-Jet system become

$$\hat{s} = M^2 = 4(E^*)^2 = x_1 x_2 s \quad (2.21)$$

$$\hat{t} = -\frac{1}{2}\hat{s}(1 - \cos\theta^*) \quad (2.22)$$

$$\hat{u} = -\frac{1}{2}\hat{s}(1 + \cos\theta^*) \quad (2.23)$$

2.4 Summary

We conclude this chapter with a brief discussion of the kinematic variables. For convenience, the most important variables are listed below.

$$x_1 = \frac{1}{2}x_T(e^{y_3} + e^{y_4}) \quad (2.24a)$$

$$x_2 = \frac{1}{2}x_T(e^{-y_3} + e^{-y_4}) \quad (2.24b)$$

$$M = \sqrt{s}\sqrt{x_1 x_2} \quad (2.24c)$$

$$\cos\theta^* = \tanh\left(\frac{y_3 - y_4}{2}\right) \quad (2.24d)$$

$$\bar{y} = \frac{y_3 + y_4}{2} = \frac{1}{2}\ln(x_1/x_2) \quad (2.24e)$$

These expressions were derived by considering the substructure of two colliding protons, and applying straightforward special relativity in the CM frame to yield experimentally accessible quantities. The high-energy hadrons contain (approximately) massless partons – quarks and gluons – that interact in a 2-body \rightarrow 2-body process, creating outgoing particles which later interact or fragment and are ultimately detected. The information obtained is used to reconstruct and gain information about the scattering subprocess.

Note that in high-energy experiments, the pseudorapidity η is more experimentally accessible than the rapidity y , as it depends only on the scattering angle, and suffices as an adequate replacement. Plots of the kinematic variables are presented in the following pages, with the rapidity y replaced by the pseudorapidity η where appropriate.

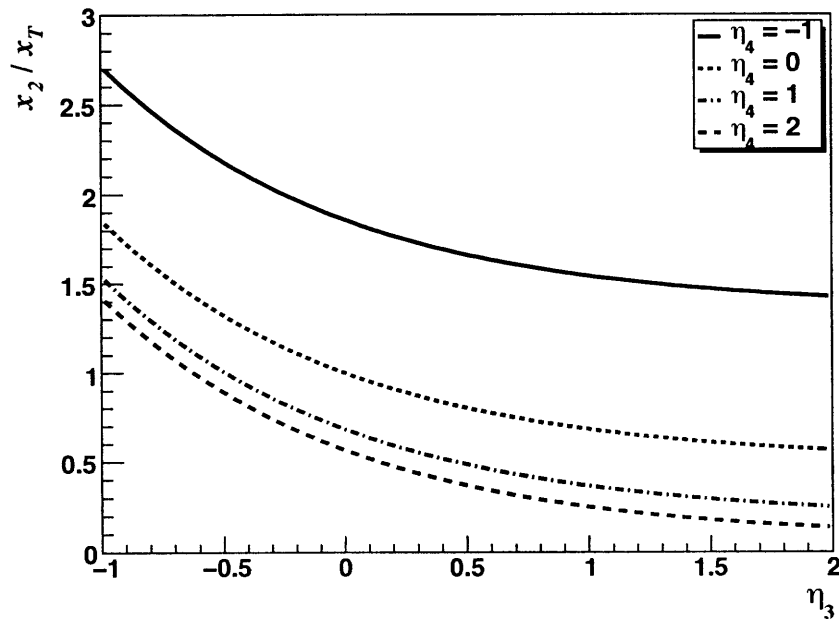
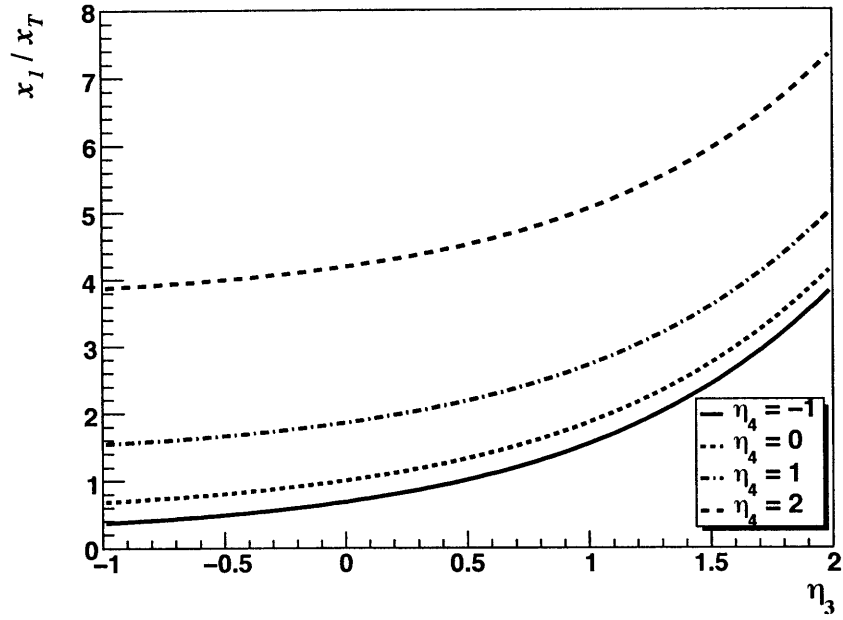


Figure 2-4: Plot of the (scaled) momentum fractions x_1 and x_2 against pseudorapidity η_3 . We only plot against η_3 as the expressions are invariant under the exchange of pseudorapidities.

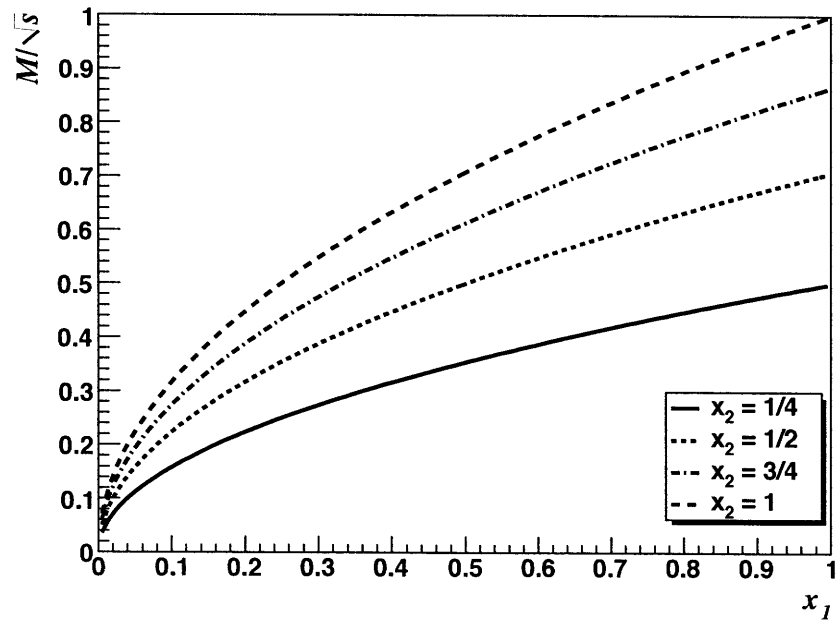


Figure 2-5: Plot of the (scaled) invariant mass M/\sqrt{s} against the full range of x_1 . We only plot against x_1 as the expression for M is invariant under the exchange x_1 and x_2 .

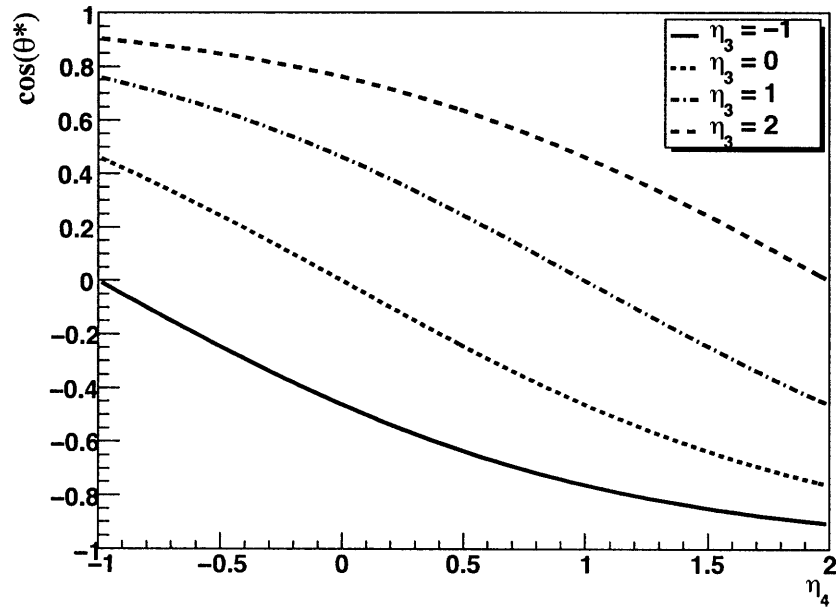
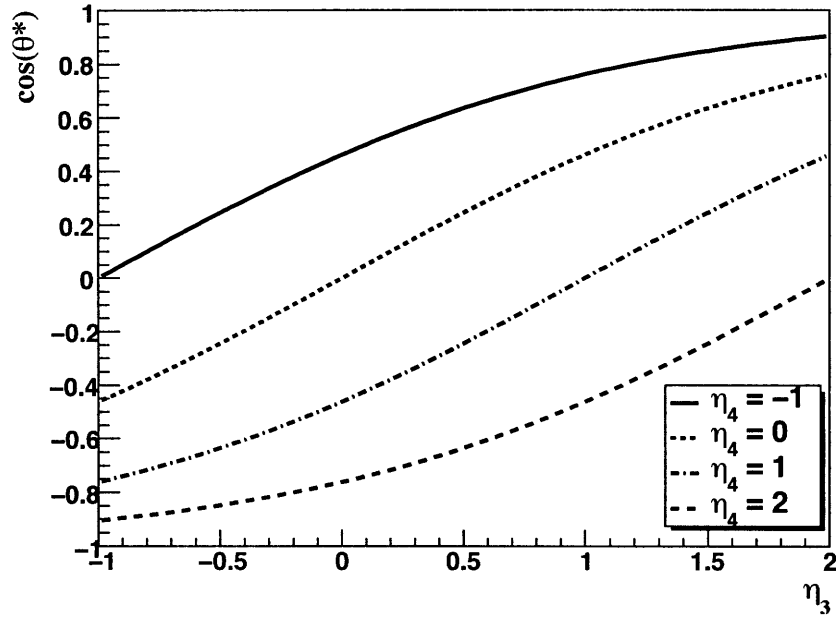


Figure 2-6: Plot of the cosine of the CM scattering angle θ^* against the observed pseudorapidities.

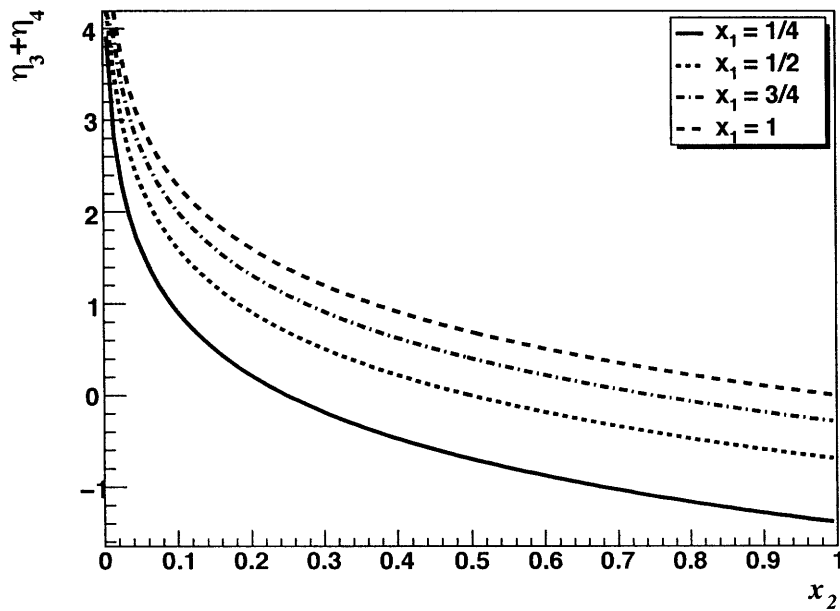
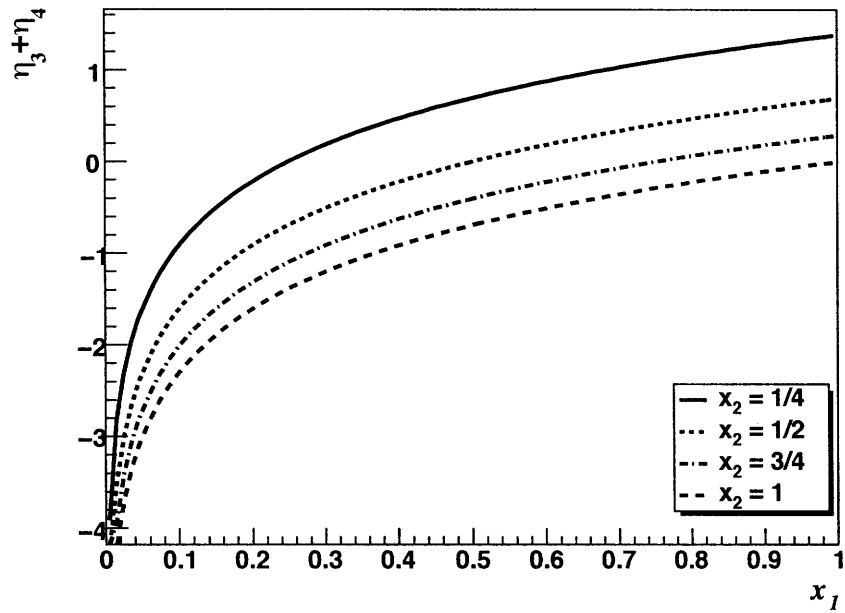


Figure 2-7: Plot of the observed sum of pseudorapidities against the momentum fractions x_1 and x_2 .

Chapter 3

A LO Δg extraction method in Di-Jet events

This chapter defines and explores the spin asymmetries to leading order. The contributing QCD subprocesses are also discussed, as well as their relative weights per given geometry. In Section 3.3 we present the leading order gluon polarization extraction method. For more details, see [3], [4] and [8].

3.1 Polarized collisions and spin asymmetry

We now return to Eq. (2.1) to discuss the specifics of the spin-dependent parton densities and cross sections. For convenience, we reproduce it below

$$\sigma(\vec{P}_1, \vec{P}_2) = \sum_{i,j} \int dx_1 dx_2 f_i(x_1, \mu^2) f_j(x_2, \mu^2) \hat{\sigma}_{ij}(\vec{p}_1, \vec{p}_2, \alpha(\mu^2), Q^2/\mu^2), \quad (3.1)$$

where the sum runs over all parton species, and where x_i are the respective hadron momentum fractions at the hard-scattering factorization scale μ . For longitudinally polarized collisions, we denote parton distribution functions (PDFs) for partons of type i and positive and negative helicities as $f_i^+(x, \mu^2)$ and $f_i^-(x, \mu^2)$ respectively. To study the proton spin structure, we examine the hadron in a helicity eigenstate described by quark and gluon helicity PDFs, denoted $\Delta f_i(x, \mu^2)$, which we define as

the difference between PDFs with positive and negative helicities

$$\Delta f_i(x, \mu^2) \equiv f_i^+(x, \mu^2) - f_i^-(x, \mu^2). \quad (3.2)$$

For example, the polarized gluon distribution is $\Delta g(x, \mu^2) \equiv g^+(x, \mu^2) - g^-(x, \mu^2)$. The total contribution to the proton spin for a given parton i is given by the integral over the full range of momentum fractions, multiplied by particular spin s_i of the parton species

$$\Delta F_i(\mu^2) \equiv s_i \int_0^1 \Delta f_i(x, \mu^2) dx. \quad (3.3)$$

With these definitions, we can express the total proton spin by

$$\int_0^1 dx \left\{ \frac{1}{2} \sum_q [\Delta q(x, \mu^2) + \Delta \bar{q}(x, \mu^2)] + \Delta g(x, \mu^2) \right\} + L(\mu^2) = \frac{1}{2}, \quad (3.4)$$

where $L(\mu^2)$ is the total orbital angular momentum of the quarks and gluons in the proton [4].

We can define a polarized cross section, analogous to Eq. (3.1), by first defining combinations of cross sections for each possible longitudinal spin setting

$$\Delta\sigma \equiv \frac{1}{4} \{(\sigma^{++} + \sigma^{--}) - (\sigma^{+-} + \sigma^{-+})\} \quad (3.5)$$

$$\Delta\hat{\sigma} \equiv \frac{1}{4} \{(\hat{\sigma}^{++} + \hat{\sigma}^{--}) - (\hat{\sigma}^{+-} + \hat{\sigma}^{-+})\} \quad (3.6)$$

so that

$$\Delta\sigma = \sum_{i,j} \int dx_1 dx_2 \Delta f_i(x_1, \mu^2) \Delta f_j(x_2, \mu^2) \Delta \hat{\sigma}_{ij}(\vec{p}_1, \vec{p}_2, Q^2/\mu^2). \quad (3.7)$$

However, experimentally, the measurable quantity that allows us to access and examine the polarized parton distributions is not simply the scattering cross section, but rather the longitudinal spin asymmetry A_{LL} , defined by

$$A_{LL} \equiv \frac{\Delta\sigma}{\sigma} = \frac{\sum_{i,j} \int dx_1 dx_2 \Delta f_i(x_1, \mu^2) \Delta f_j(x_2, \mu^2) \hat{\sigma}_{ij}(\hat{a}_{LL})_{ij}}{\sum_{i,j} f_i(x_1, \mu^2) f_j(x_2, \mu^2) \hat{\sigma}_{ij}}, \quad (3.8)$$

Class	Process(s)	$\hat{a}_{LL}(s, t, u)$	$\hat{a}_{LL}(\cos \theta^*)$
A	$gg \rightarrow gg$	$\frac{2\frac{\hat{s}^2}{\hat{t}\hat{u}} + \frac{\hat{t}\hat{u}}{\hat{s}^2} - 3}{3 - \frac{\hat{s}\hat{u}}{\hat{t}^2} - \frac{\hat{s}\hat{t}}{\hat{u}^2} - \frac{\hat{t}\hat{u}}{\hat{s}^2}}$	$\frac{(1 - \cos^4 \theta^*)(7 + \cos^2 \theta^*)}{(3 + \cos^2 \theta^*)^2}$
B	$qq \rightarrow qq$	$\frac{\hat{t}^2 + \hat{u}^2 - \frac{2}{3}\hat{t}\hat{u} - \left(\frac{\hat{t}^4 + \hat{u}^4}{\hat{s}^2}\right)}{\hat{t}^2 + \hat{u}^2 - \frac{2}{3}\hat{t}\hat{u} + \left(\frac{\hat{t}^4 + \hat{u}^4}{\hat{s}^2}\right)}$	$\frac{5 - 3 \cos^4 \theta^* - 2 \cos^2 \theta^*}{11 + 3 \cos^4 \theta^* + 34 \cos^2 \theta^*}$
C	$qq' \rightarrow qq'$ $q\bar{q}' \rightarrow q\bar{q}'$ $qg \rightarrow qg$ $qg \rightarrow q\gamma$	$\frac{\hat{s}^2 - \hat{u}^2}{\hat{s}^2 + \hat{u}^2}$	$\frac{4 - (1 + \cos \theta^*)^2}{4 + (1 + \cos \theta^*)^2}$
D	$q\bar{q} \rightarrow q\bar{q}$	$\frac{\left(\frac{\hat{s}^4 - \hat{t}^2}{\hat{u}^2}\right) - (\hat{s}^2 + \hat{t}^2 - \frac{2}{3}\hat{s}\hat{t})}{\left(\frac{\hat{s}^4 + \hat{t}^4}{\hat{u}^2}\right) + (\hat{s}^2 + \hat{t}^2 - \frac{2}{3}\hat{s}\hat{t})}$	$\frac{13 - (3 \cos^4 \theta^* - 5 \cos^3 \theta^* + 10 \cos^2 \theta^* + 8 \cos \theta^*)}{35 + (3 \cos^4 \theta^* - 5 \cos^3 \theta^* + 10 \cos^2 \theta^* + 8 \cos \theta^*)}$
E	$gg \rightarrow q\bar{q}$ $q\bar{q} \rightarrow gg$ $q\bar{q} \rightarrow g\gamma$ $q\bar{q} \rightarrow q'\bar{q}'$ $q\bar{q} \rightarrow l\bar{l}$	-1	-1

Table 3.1: Listed above are the (massless) partonic asymmetries, given in terms of Mandelstam variables and the CM scattering angle θ^* , for each given class of processes. The relative contributions to the total spin asymmetry for a given geometry are shown in Fig. 3-1, and more explicitly in Fig. 3-2.

where $(\hat{a}_{LL})_{ij} = \Delta\hat{\sigma}_{ij}/\hat{\sigma}_{ij}$ is the subprocess partonic spin asymmetry.¹

3.2 Contributions from partonic spin asymmetry

We begin by analyzing the partonic spin asymmetry \hat{a}_{LL} in leading order (LO). At this order, \hat{a}_{LL} is calculable in perturbative QCD and the results are given in Table 3.1. Plotting \hat{a}_{LL} for various processes against the cosine of the CM scattering angle gives the relative weights (contributions) to the total spin asymmetry A_{LL} for a given product geometry.

Examining Fig. 3-1, we can find the particular geometries corresponding to the maximum contribution for a given process. For classes A and B, the distribution of \hat{a}_{LL} is symmetric, and hence we expect those processes to become important for a CM

¹The spin subprocess asymmetry \hat{a}_{LL} is often referred to as the *analyzing power*.

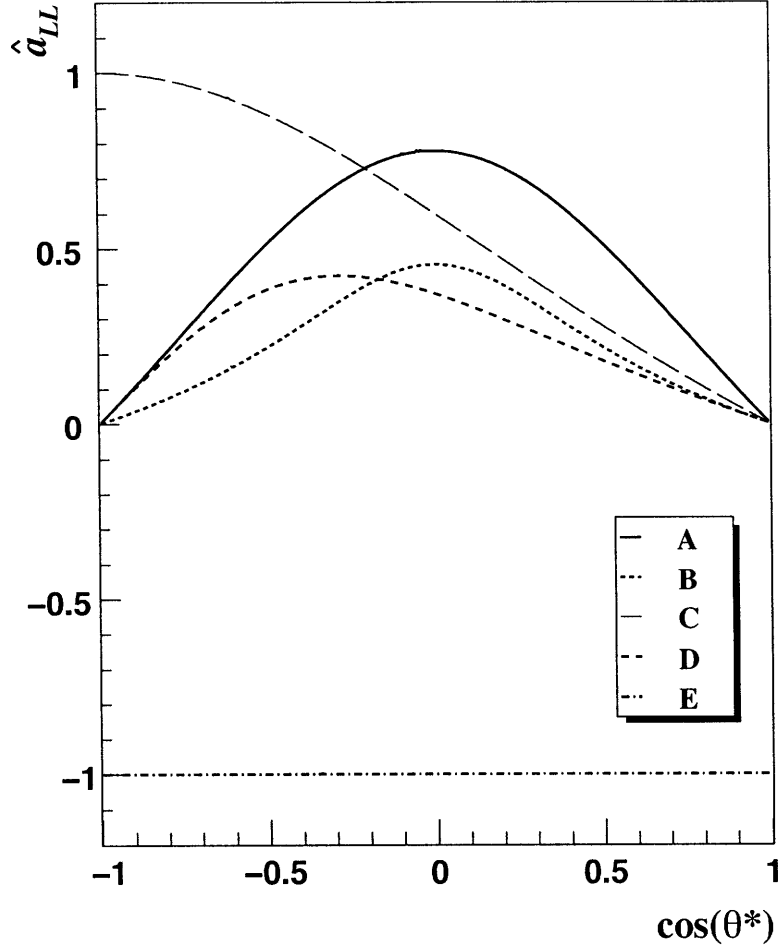


Figure 3-1: Plot of the (massless) partonic asymmetry \hat{a}_{LL} against cosine of CM scattering angle θ^* for each given class of processes A, B, C, D, and E (see Table 3.1). Each line gives the relative weight towards the total spin asymmetry A_{LL} .

scattering angle around $\theta^* = 90^\circ$. Class C processes have a maximum contribution for $\theta^* = 180^\circ$. The maximum for Class D processes is less immediate as it does not possess a nice symmetry, but referencing \hat{a}_{LL} from Table. 3.1 and performing a quick calculation, we find the maximum to occur at

$$\cos \theta^* = \frac{1}{3} \left\{ 2 + \left(\sqrt{257} - 16 \right)^{1/3} - \left(\sqrt{257} - 16 \right)^{-1/3} \right\} \approx -0.2870 \implies \theta^* \approx 107^\circ$$

Notice that there is always a constant background due to class E processes. These critical angles, including the respective symmetric angles 180° apart, allow us to

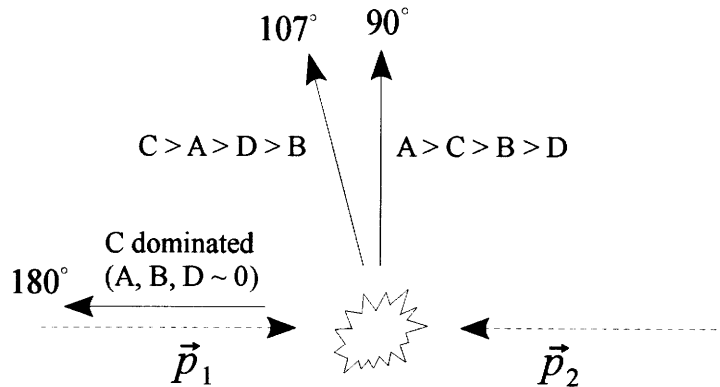


Figure 3-2: Relative contributions and geometries for various classes of processes for given key angles. Note that the (massless) Di-Jet system produces symmetric product jets 180° apart (not shown).

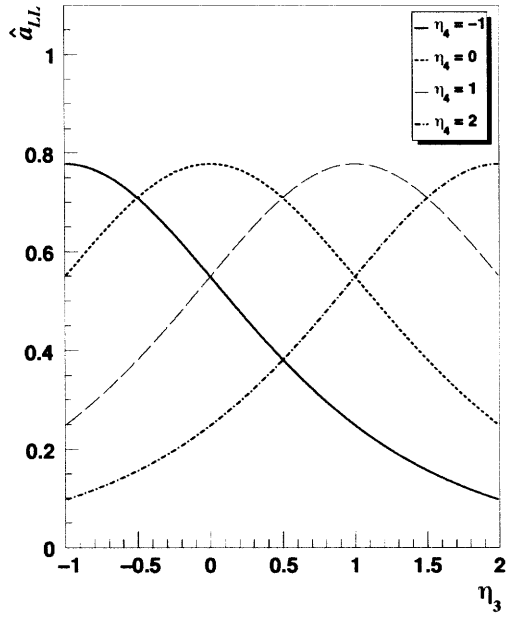
more easily sort out collision processes in the detector by giving regions in which known classes of processes dominate over others. An explicit representation of these conclusions is given in Fig. 3-2.

To shed more light on the partonic asymmetries, we express them in terms of another experimentally accessible set of parameters, the product parton pseudorapidities. The plots are shown in Fig. 3-3. Although the corresponding geometries and scattering angles are less obvious, the plots indicate what combinations of product rapidities will generate the largest partonic spin asymmetry.

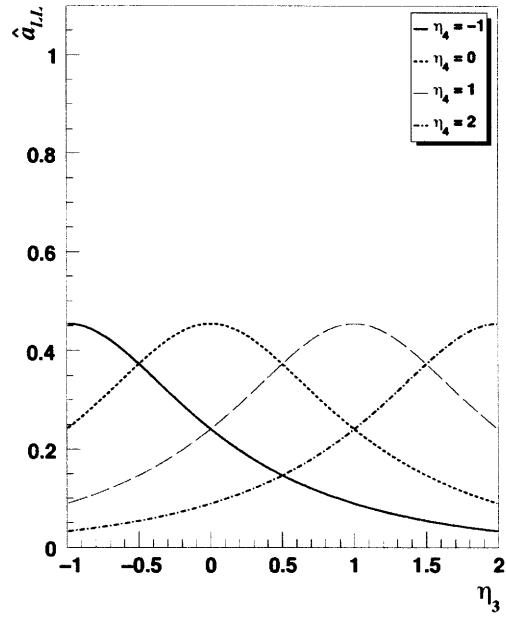
3.3 Extraction of Δg from partonic asymmetry

For this analysis, we consider *back-to-back* Di-Jets; that is, we consider regions for which $x_1 = x_2 = x$. From Equations (2.24a) through (2.24e) we see that for back-to-back Di-Jets, $y_4 = -y_3$ and $\cos \theta^* = \tanh y_3$. Now, we plot the total spin asymmetry A_{LL} against the observed $M/\sqrt{s} = \sqrt{x_1 x_2} = x$ to give A_{LL} as a function of x . Typical plots of A_{LL} vs. M/\sqrt{s} showing the statistical precision are given in Fig. 3-4 (for more details, see [7] and [14]).

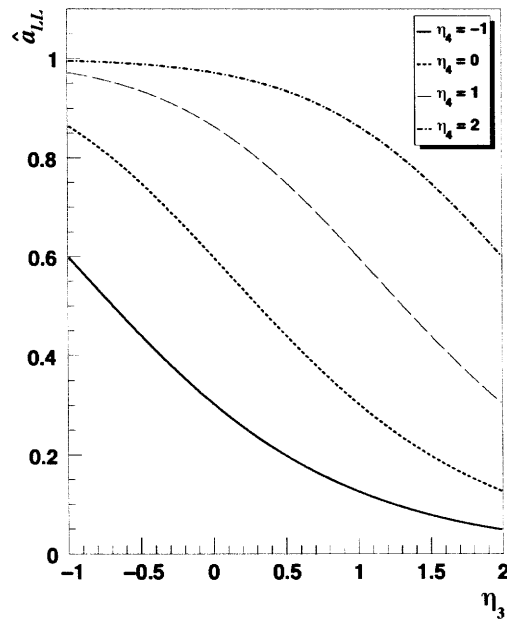
Assuming the parton kinematics can be accurately reconstructed from the collider data, we can bin the events in the back-to-back momentum fraction x of the hard



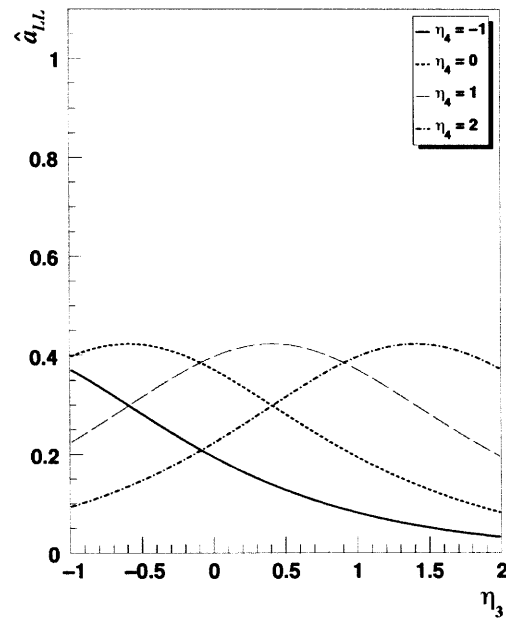
Class A processes



Class B processes



Class C processes



Class D processes

Figure 3-3: Plot of the (massless) partonic asymmetry \hat{a}_{LL} against the pseudorapidity η_3 for several different values of η_4 for the given classes of processes (defined in Table 3.1).

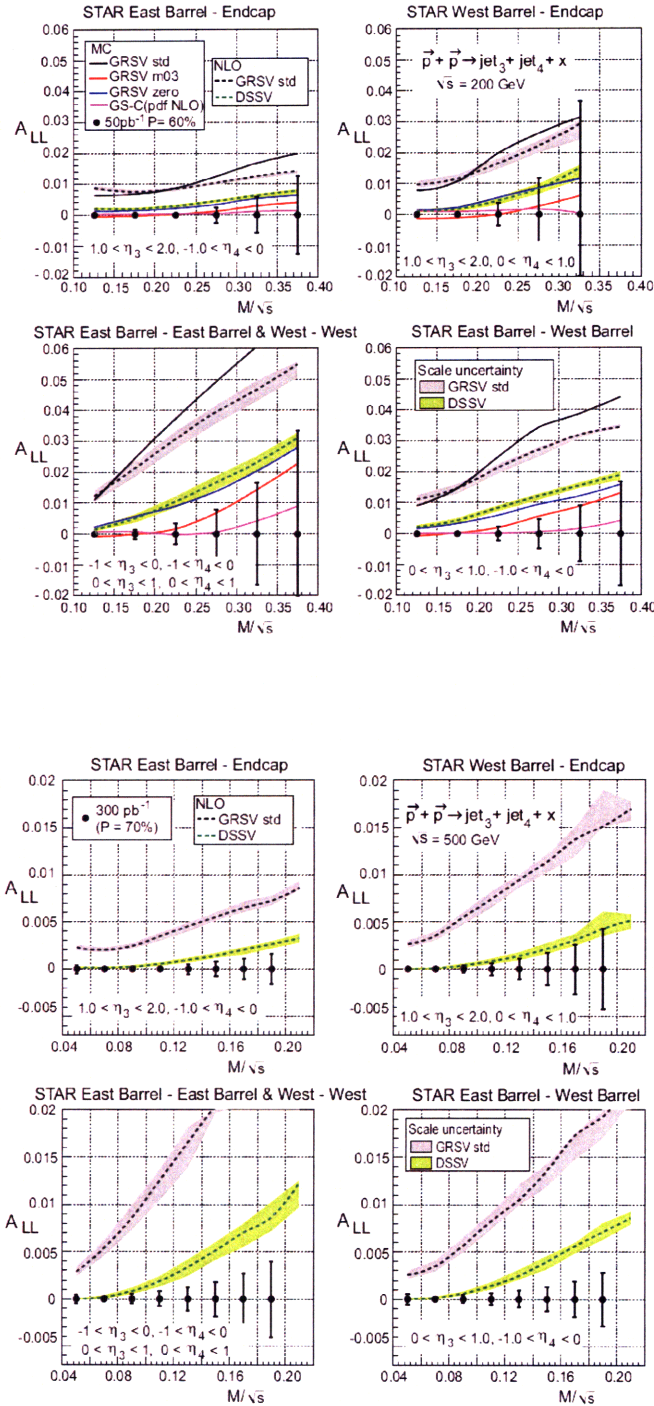


Figure 3-4: Plots of A_{LL} against the invariant mass M/\sqrt{s} for Di-Jets at $\sqrt{s} = 200$ GeV (upper) and $\sqrt{s} = 500$ GeV (lower), highlighting the statistical precision given various geometrical configurations. (From [7])

scattering process. For a particular bin $x \in [x_k, x_{k+1}]$, we can rewrite Eq. (3.8) as

$$A_{LL} = \frac{1}{\sigma} \int_{x_k}^{x_{k+1}} dx_1 \int_{x_k}^{x_{k+1}} dx_2 \left\{ \hat{a}_{gg}(x_1, x_2) \Delta g(x_1) \Delta g(x_2) + \hat{a}_{qg} \Delta g(x_1) \Delta q(x_2) \right. \\ \left. + \hat{a}_{qq'}(x_1, x_2) \Delta q(x_1) \Delta q'(x_2) \right\}, \quad (3.9)$$

where $\hat{a}_{ij} \equiv \hat{\sigma}_{ij} (\hat{a}_{LL})_{ij}$ are the products of the (massless) partonic cross sections and corresponding partonic asymmetries for each given process, which are either calculable or at least parameterizable, and $\Delta q(x)$ represents the total quark distribution function, absorbing both quark and anti-quark contributions.

Now, consider the Taylor expansion of $\Delta g(x)$ about the point $\bar{x} \in [x_k, x_{k+1}]$

$$\Delta g(x) = \Delta g(\bar{x}) + \left. \frac{d\Delta g}{dx} \right|_{\bar{x}} (x - \bar{x}) + \frac{1}{2!} \left. \frac{d^2\Delta g}{dx^2} \right|_{\bar{x}} (x - \bar{x})^2 + \mathcal{O}((x - \bar{x})^3) \quad (3.10)$$

Note that since we are choosing an arbitrary bin $[x_k, x_{k+1}]$ that in general is not centered at zero, we do not set $\bar{x} = 0$. Now, consider the $\Delta g(x_1)\Delta g(x_2)$ term in Eq. (3.9). Plugging in the Taylor expansion, we have

$$\left(\Delta g(\bar{x}) + \left. \frac{d\Delta g}{dx} \right|_{\bar{x}} (x_1 - \bar{x}) + \dots \right) \left(\Delta g(\bar{x}) + \left. \frac{d\Delta g}{dx} \right|_{\bar{x}} (x_2 - \bar{x}) + \dots \right) \\ = (\Delta g(\bar{x}))^2 + \Delta g(\bar{x}) \left. \frac{d\Delta g}{dx} \right|_{\bar{x}} [(x_1 - \bar{x}) + (x_2 - \bar{x})] + \mathcal{O}((x - \bar{x})^2). \quad (3.11)$$

Under the integral, the first term becomes

$$\int_{x_k}^{x_{k+1}} dx_1 \int_{x_k}^{x_{k+1}} dx_2 \hat{a}_{gg}(x_1, x_2) \left\{ (\Delta g(\bar{x}))^2 + \Delta g(\bar{x}) \left. \frac{d\Delta g}{dx} \right|_{\bar{x}} [(x_1 - \bar{x}) + (x_2 - \bar{x})] + \mathcal{O}((x - \bar{x})^2) \right\} \\ = \int_{x_k}^{x_{k+1}} dx_1 \int_{x_k}^{x_{k+1}} dx_2 \hat{a}_{gg}(x_1, x_2) \left\{ (\Delta g(\bar{x}))^2 + 2\Delta g(\bar{x}) \left. \frac{d\Delta g}{dx} \right|_{\bar{x}} (x_1 - \bar{x}) + \mathcal{O}((x - \bar{x})^2) \right\},$$

where we have exploited the exchange symmetry between x_1 and x_2 in $\hat{a}_{gg}(x_1, x_2)$ and in the limits of the integral. Notice that the leading error term can be eliminated by requiring that \bar{x} satisfy

$$\int_{x_k}^{x_{k+1}} dx_1 \int_{x_k}^{x_{k+1}} dx_2 \hat{a}_{gg}(x_1, x_2) (x_1 - \bar{x}) = 0. \quad (3.12)$$

Now, we return to the remaining terms in Eq. (3.9). The second term contains one factor of $\Delta g(x_1)$, and inserting the Taylor series yields

$$\int_{x_k}^{x_{k+1}} dx_1 \int_{x_k}^{x_{k+1}} dx_2 \hat{a}_{qg}(x_1, x_2) \Delta q(x_2) \left\{ \Delta g(\bar{x}) + \frac{d\Delta g}{dx} \Big|_{\bar{x}} (x_1 - \bar{x}) + \mathcal{O}((x_1 - \bar{x})^2) \right\}.$$

Therefore, by assigning

$$c_1 = \frac{1}{\sigma} \int_{x_k}^{x_{k+1}} dx_1 \int_{x_k}^{x_{k+1}} dx_2 \hat{a}_{qg}(x_1, x_2) \quad (3.13)$$

$$c_2 = \frac{1}{\sigma} \int_{x_k}^{x_{k+1}} dx_1 \int_{x_k}^{x_{k+1}} dx_2 \left\{ \hat{a}_{qg}(x_1, x_2) \Delta q(x_2) + 2\hat{a}_{gg} \frac{d\Delta g}{dx} \Big|_{\bar{x}} (x_1 - \bar{x}) \right\} \quad (3.14)$$

$$c_3 = \frac{1}{\sigma} \int_{x_k}^{x_{k+1}} dx_1 \int_{x_k}^{x_{k+1}} dx_2 \left\{ \hat{a}_{qq'}(x_1, x_2) \Delta q(x_1) \Delta q'(x_2) + \hat{a}_{qg}(x_1, x_2) \Delta q(x_2) \frac{d\Delta g}{dx} \Big|_{\bar{x}} (x_1 - \bar{x}) \right\}, \quad (3.15)$$

we reduce the problem of extracting the gluon distribution to that of simply solving the quadratic formula

$$\boxed{A_{LL}(x) = c_1 (\Delta g(x))^2 + c_2 \Delta g(x) + c_3}, \quad (3.16)$$

where all variables A_{LL} and c_i are determined through measurements and known calculations.

The general strategy then, would be to bin the data A_{LL} against $M/\sqrt{s} = x$, and for each bin, iterate the calculation in Eq. (3.16) so that the errors given in c_1 and c_2 (terms proportional to $d\Delta g/dx$) are minimized – either by exploiting Eq. (3.12) or another standard. To further refine the extraction, the bin calculation could be iterated further to minimize the error in the next order in the integral, represented above by $\mathcal{O}((x - \bar{x})^2)$, which can be easily expressed explicitly by calculating more terms in the Taylor series product in (3.11). Through this method we should be able to fairly accurately, and efficiently, deduce the shape of the polarized gluon distribution, without any assumptions on the functional form.²

²Except of course that it be continuous and differentiable.

Chapter 4

Summary and further work

The “spin crisis problem” remains a fascinating problem that tests the foundation of QCD. In the previous chapters, we developed a method to extract the polarized gluon distribution Δg from the double spin asymmetry A_{LL} , taking what seemed to be a rather intractable problem into an almost trivial calculation: solving the quadratic formula. The errors due to the Taylor series truncation are easily determined – the error in each truncation is less than the maximum size of the next order term, and the propagation of the errors through the quadratic are straightforward. What remains to be done is to apply the method to simulated data, with a given functional form for Δg , to see how well Δg can be recovered. This step is in process at the time of writing. If successful, the method will be applied to actual collider data to help illuminate the momentum dependence of the gluon polarization.

Bibliography

- [1] B. I. Abelev et al. Longitudinal double-spin asymmetry and cross section for inclusive jet production in polarized proton collisions at $s^{**}(1/2) = 200$ -GeV. *Phys. Rev. Lett.*, 97:252001, 2006.
- [2] B. I. Abelev et al. Longitudinal double-spin asymmetry for inclusive jet production in p+p collisions at $\sqrt{s}=200$ GeV. *Phys. Rev. Lett.*, 100:232003, 2008.
- [3] S.D. Bass. *The Spin Structure of the Proton*. World Scientific, 2008.
- [4] G. Bunce et al. *Ann. Rev. Nucl. Part. Sci. Nucl.*, 119:3, 2000.
- [5] D. de Florian, Rodolfo Sassot, and G.A. Navarro. *Phys. Rev.*, D71:094018, 2005.
- [6] Daniel de Florian, Rodolfo Sassot, Marco Stratmann, and Werner Vogelsang. arxiv:0804.0422 [hep-ph].
- [7] G. Bunce *et al.* (rhic spin, phenix, star collaborations) plans for the rhic spin physics program. 2008.
- [8] R.K. Ellis *et al.* *QCD and Collider Physics*. Cambridge, 1996.
- [9] J. Ashman *et al.* [European Muon Collaboration]. *Phys. Lett.*, B206:364, 1988.
- [10] K.H. Ackermann *et al.* (STAR Collaboration). *Nucl. Instrum. Methods A.*, 2003.
- [11] M. Glueck, E. Reya, M. Stratmann, and W. Vogelsang. Models for the polarized parton distributions of the nucleon. *Phys. Rev.*, D63:094005, 2001.
- [12] D. Griffiths. *Introduction to Elementary Particles*. Wiley, 1987.
- [13] M.E. Peskin and D.V.Schroeder. *An Introduction to Quantum Field Theory*. Westview, 1995.
- [14] B. Surrow. (For the STAR Collaboration) Status and prospects of di-jet production in high-energy polarized proton-proton collisions at $\sqrt{s}=200$ GeV.
- [15] B. Surrow. *J. Phys. Conf. Ser.*, 2008.